Ambient noise tomography of northern Borneo reveals evidence of subduction and post-subduction processes.

J. Fone[1], N. Rawlinson[1], S. Pilia[2], A. Gilligan[3], D. G. Cornwell[3], F. Tongkul[4]

[1]Bullard Laboratories, University of Cambridge, Cambridge, UK
[2]College of Petroleum Engineering and Geosciences, King Fahd University of Petroleum and Minerals, Dhahran, Saudi Arabia
[3]Department of Geology and Geophysics, University of Aberdeen, Aberdeen, UK
[4]Faculty of Science and Natural Resource, Universiti of Malaysia Sabah, Kota Kinabalu, Malaysia

Key Points:

- New 3D shear wave model of crust in northern Borneo from ambient seismic noise tomography illuminates post subduction setting
- Velocity structure underlying the Crocker Range is consistent with underthrust continental crust following proto South China sea subduction
- Velocity structure in the southeast consistent with widespread igneous intrusion and underthrusting of mantle wedge sediments

Corresponding author: J. Fone, jwf39@cam.ac.uk

Abstract

The region of northern Borneo in South East Asia sits within a post-subduction setting formed by the recent termination of two sequential but opposed subduction systems. In this study we use seismic data from a recent temporary array deployment to image the crustal velocity structure beneath northern Borneo using a two-stage Bayesian trans-dimensional tomography scheme, in which period dependent phase velocity maps are first generated, and then used to build a 3-D shear wave model through a series of 1-D inversions. In the second stage, we also apply an Artificial Neural Network to solve the 1D inverse problem, which results in a smoother 3-D model compared to the TransD approach without sacrificing data fit. Our shear wave velocity model reveals a complex crustal structure. Under the Crocker Range, a heterogeneous velocity structure likely represents remnants of early Miocene subduction, including underthrust continental crust from subsequent continent-continent collision. In the east we observe high velocities that are interpreted to be igneous rocks in the crust generated by melting due to mid Miocene Celebes Sea subduction and later decompression melting as well as a low velocity zone that could represent underthrust sediment or duplexes from Celebes Sea subduction. A low velocity zone in the lower crust is present in a region of apparent crustal thinning. Our preferred explanation for this anomaly is remnant thermal upwelling within a failed rift that represents the on-shore continuation of the extension of the Sulu Sea, most likely caused by rollback of the Celebes Sea slab.

Plain Language Summary

The island of Borneo is located in South East Asia. Although some distance from active plate boundaries, its northern tip has a complex tectonic history over the last ∼30 million years, with sequential subduction (one tectonic plate descending into the mantle beneath an adjacent plate) from the north and south that that ceased ∼9 million years ago. In this study we use data recorded by seismometers to image the properties of the rocks in the crust underneath northern Borneo. Rather than use earthquake signals, we instead use ambient seismic noise, which is continuous low amplitude ground motion largely produced by ocean waves. This data can be used to produce a 3-D model of shear wave (transverse elastic waves) velocity structure. From this model we observe evidence of continent-continent collision following subduction of the proto-South China Sea. We see evidence of rock that melted during subduction of the Celebes Sea slab that has re-solidified following subduction termination. We also see evidence of a high temperature anomaly at depth in the centre of our model, which supports the idea of crustal extension in central Borneo driven by opening of the Sulu Sea in response to retreat of the subducting Celebes Sea slab.

1 Introduction

Northern Borneo encompasses the Malaysian state of Sabah and is located in the intra-plate region of southeast Asia (Figure 1), with the nearest subduction zone lying beneath the Northern Sulawesi trench over 500 km to the south east. Despite its remoteness from plate boundaries, northern Borneo is geologically very complex and exhibits signs of ongoing tectonic activity, likely related to the recent termination of two opposed subduction systems (Hall, 2013). Beneath north-west Borneo, subduction of the Proto-South China Sea terminated in the Early Miocene (∼21 Ma) with the onset of continent-continent collision involving the Dangerous Grounds block; this caused much of northern Borneo to uplift and deform as part of the Sabah Orogeny (Hall, 2013; Hutchison et al., 2000; Hall, 1996; Tongkul, 1994). This is believed to have been followed by north-west directed subduction of the Celebes Sea beneath the Sulu Arc to the southeast, which began at ∼21 Ma and was followed by rifting of the Sulu Sea due to subduction rollback (Hall, 2013). The subduction of the Celebes Sea is thought to have terminated at ∼9

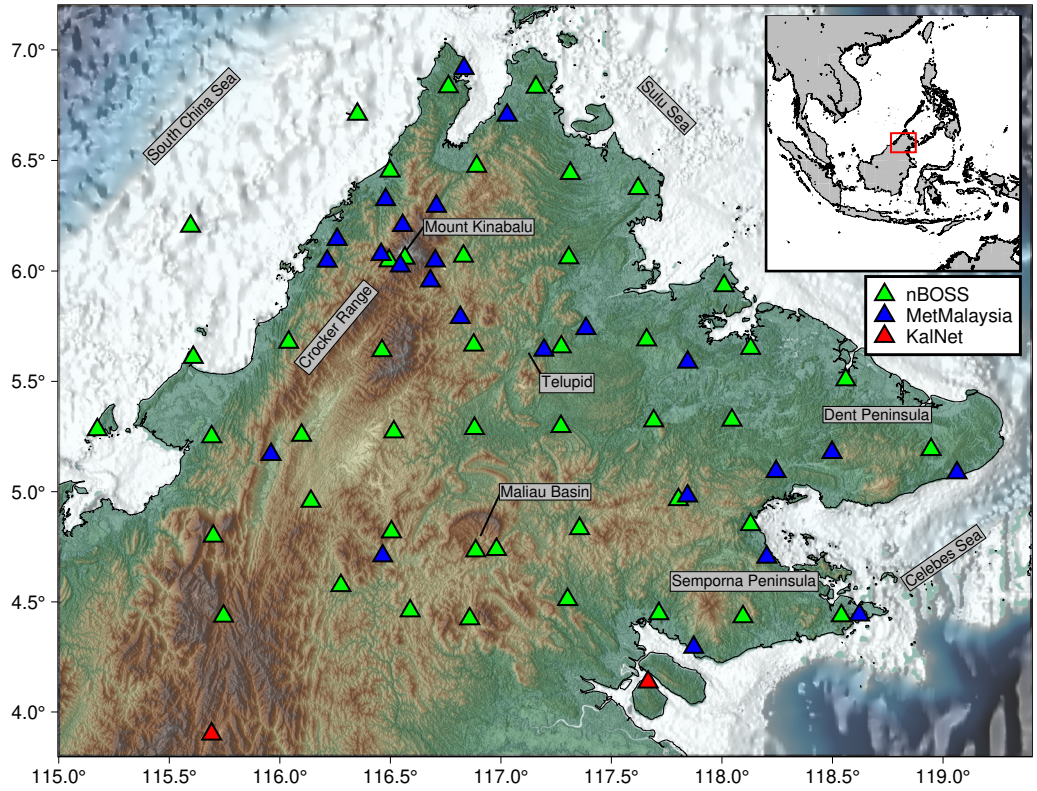

Figure 1. Location of seismic stations (coloured triangles) and networks (see key) used in this study. Inset map shows the location of northern Borneo in the greater southeast Asia region.

Ma as recorded by the cessation of arc magmatism (Lai et al., 2021). Linang et al. (2022) propose that this sequence of events constitutes subduction polarity reversal or SPR involving continental lithosphere as opposed to oceanic arcs or oceanic plateau that are normally invoked to produce a polarity switch (Almeida et al., 2022; Wang et al., 2022).

The complicated tectonic history of northern Borneo described above is expressed in a variety of different ways in the surface geology and landscape of the region (Figure 1). Major surface features include the Crocker Range in the northwest, which formed during the Sabah Orogeny in the Miocene, as well as Mt Kinabalu, an exposed granitic intrusion within the Crocker Range that was emplaced ~7 Ma and subsequently uplifted, which now sits at the surface with an elevation of 4095 m, much higher than the majority of the Crocker Range with ~1500 m elevation (Cottam et al., 2010). There are also large sedimentary basins in the region including unusual elevated circular basins in the south, such as the Maliau Basin, which is believed to have formed from deltaic sediments in the mid to late-Miocene but was subsequently uplifted in the Pliocene (3-5 Ma) (Balaguru et al., 2003). The peak of the surrounding escarpment now sits at 1675 m above sea level and the underlying basin sediments are thought to be up to 6000 m thick (Balaguru et al., 2003). One of the challenges in trying to unravel the geology and tectonics of northern Borneo is that much of the surface is masked by thick tropical regolith and dense vegetation, which severely limits outcrop. This leaves many basic questions to be answered including the extent to which compressional (Morley et al., 2011; Morley & Back, 2008; Tongkul, 1997) or extensional (Pilia et al., 2023a, 2023b; Hall, 2013) tectonics control the evolution of the lithosphere.

There have been a number of previous geophysical studies that have included northern Borneo, many of which involve the generation of regional velocity models of southeast Asia from seismic imaging. Although limited in resolution, they consistently reveal a high velocity feature in the upper mantle at around ∼100-300 km depth, which is generally attributed to remnant slabs (Laat et al., 2023; Wehner et al., 2022; Zenonos et al., 2020; Hall & Spakman, 2015; Tang & Zheng, 2013). More recently, targeted seismic studies have been performed using data from the northern Borneo Orogeny Seismic Survey (nBOSS) experiment (Pilia et al., 2019). Imaging of the mantle using teleseismic P and S wave arrival time tomography has been performed by Pilia et al. (2023a), who found two distinct anomalies, one of which was attributed to a proto-South China Sea slab remnant and the other to a lithospheric drip that detached from beneath the Semporna Peninsula. Imaging of the mantle by 2-plane wave surface wave tomography was performed by Greenfield et al. (2022), who found thin lithosphere beneath the Semporna Peninsula, further supporting the idea that mantle lithosphere has been removed from this region. Detachment of lithosphere in this way has been shown, via numerical modelling, to cause extension and thinning of the crust, subcrustal melting and exhumation (Pilia et al., 2023b). Linang et al. (2022) found evidence for Sulu Sea extension continuing on-shore in northern Borneo by imaging crustal thickness variations using virtual deep seismic sounding. Bacon et al. (2022) measured lithospheric anisotropy using XKS splitting and found that orientations of the fast axis of anisotropy were predominantly parallel to the Crocker Range in western northern Borneo, suggesting that anisotropy is dominated by recent continental collision. Fast axis orientations orthogonal to the opening of the Sulu Sea in central northern Borneo further support the idea of Sulu Sea extension propagating on-shore. Receiver functions have also been produced for the nBOSS network stations by Gilligan et al. (2023) and subsequently inverted for S wave velocity structure, which revealed complex crustal structure in the western region of northern Borneo, which was interpreted to be underthrust Dangerous Grounds crust. Thinner crust likely related to the rollback of the Celebes Sea slab and lower velocities beneath the Semporna Peninsula that may be attributed to the previously mentioned lithospheric detachment were also delineated.

In this study we apply two-step surface-wave Ambient Noise Tomography (ANT) to data from the recent temporary nBOSS deployment to produce a new crustal scale shear wave velocity model of the region. Our aim is to study how the complex tectonic history from the early Neogene has imprinted itself on the velocity structure of the crust, thereby enabling a better understanding of its origins and evolution. We aim to use the higher lateral resolution inherent in ANT to image new features not recovered in studies such as Gilligan et al. (2023) and illuminate shallower structures than were imaged in Greenfield et al. (2022). We follow a method similar to Pilia et al. (2020), but also apply a new method for improving the two-step inversion process of ANT by using a Neural Network in the 1D inversions, which reduces sensitivity to unphysical dispersion curves, and enhances the quality of the final model that is produced.

2 Data and methods

2.1 Deployment and data

Data for this study were collected primarily during the northern Borneo Orogeny Seismic Survey (nBOSS), which was a temporary deployment of 46 broadband seismic stations throughout northern Borneo between 2018 and 2020 (Pilia et al., 2019). A mixture of sensors with frequency responses from 30 seconds to 100 Hz (Guralp 6TD) and 60 seconds to 100 Hz (Guralp 3ESP) were used in the deployment. This was augmented by 24 MetMalaysia permanent stations with a frequency response between 120 seconds to 50 Hz (STS-2) as well as two stations deployed in northern Kalimantan (Guralp 6TD). In total, 72 broadband seismometers with between 20-24 months of continuous recordings were available for surface wave ambient noise tomography. The location of the complete station network is shown in Figure 1. The data were generally of average to good

quality for surface wave ambient noise due in part to the proximity of the sea on three sides, which provided strong signal from oceanic microseisms. The cross correlations that were used in picking had a signal to noise ratio (SNR) of 92, as defined by taking the ratio of the average power of the cross correlation between 1.5 and 4.5 km/s moveout over the average power of the remaining wavetrain. However, the signals were not as clean as expected. Many of the stations, especially in the south-east, were deployed in palm oil plantations where anthropogenic noise may have overprinted at least parts of the frequency range of interest. More importantly, a number of deep sedimentary basins exist in central Sabah, which may generate ringing effects that manifest as an inhomogeneous noise source within our array. According to Hanasoge (2013) a noise source within the array would result in signal occurring at or around zero delay time, which we see very strongly in our cross correlations shown in Figure 2.

2.2 Extracting dispersion curves

In order to obtain phase velocity dispersion curves for each station pair we follow the Frequency Time Analysis (FTAN) method described in Yao et al. (2006). We first use the python package MSNOISE (Lecocq et al., 2014) to compute daily inter-station cross-correlations that were subsequently stacked with non-linear phase-weighted stacking to reduce amplitude sensitivity compared to linear stacking, thus diminishing the effect of incoherent noise in the final set of cross-correlations (Pilia et al., 2020; Ventosa et al., 2017), which are shown in panel A in Figure 2. The cross-correlations were then converted into Empirical Green's Functions (EGF) using the symmetric component of the cross correlations. The EGFs represent an estimate of the impulse response of the Earth to a surface wave traveling between two stations. The time domain EGFs were then converted into FTAN images that are made by narrow band filtering over a range of central periods and a width in each case equal to 0.4 times the central period (Volk et al., 2021; Volk, 2020). Each of the FTAN images were then converted pixel by pixel to have a value of one at local maxima along the velocity axis and a value of zero everywhere else, highlighting the peaks representing different possible curves in the given FTAN image. These were then summed together for each station pair and smoothed, resulting in the image shown in panel B in Figure 2. This shows a peak in the velocity-period domain that represents a regional dispersion curve that can be used to guide the picking of each interstation dispersion curve. Panel C in Figure 2 shows an example FTAN image that includes the regional curve to help identify the correct peak. We limited the maximum period that could be picked by making sure the inter-station distance was greater than 2 wavelengths at that period (Luo et al., 2015). This approach was used to obtain fundamental mode Rayleigh wave dispersion curves in the period range 2-40 seconds by manually picking the correct dispersion curve from each FTAN image. After picking, the resultant dataset for use in tomography comprised 1172 dispersion curves.

2.3 2D tomography

Period-dependent phase velocity maps were obtained via inversion of the dispersion data at each period using the 2D trans-dimensional trees tomography method of Hawkins and Sambridge (2015). This approach uses a reversible jump Markov Chain Monte Carlo (rj-MCMC, Green, 1995) method to sample models over a tree structure that allows for varying levels of complexity within the final ensemble. The tree structure works by having the model described by sets of wavelet parameters that can be thought of as nodes in the branches of a tree. At each layer up the tree the node splits into a set of finer wavelet parameters (with up to 7 hierarchical layers), thus allowing a model to be described as a combination of coarse parameters and fine parameters depending on the shape of the tree. At each iteration, one or more of the parameters in the tree can be perturbed, new nodes can be birthed and existing nodes can die, resulting in the total number of parameters being allowed to change throughout the inversion. The number of parameters and

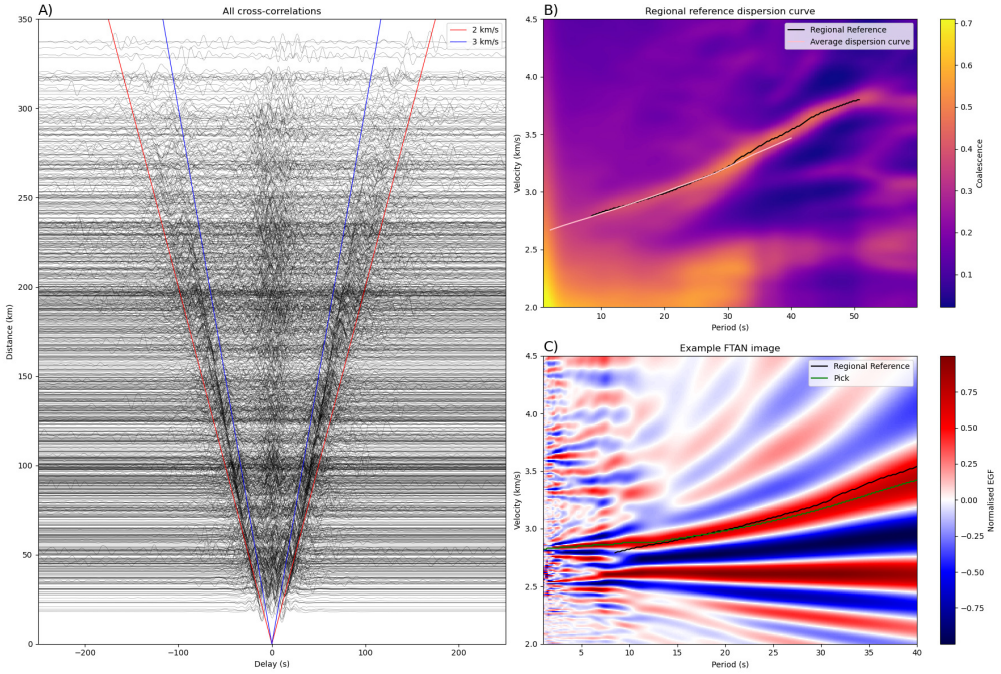

Figure 2. (A): All cross correlations from which dispersion curves were extracted plotted as interstation distance vs delay time, filtered with a broadband filter between 8-40s. Red and blue lines show the move-out of 2 km/s and 3 km/s surface waves respectively. (B): Regional reference dispersion curve formed by stacking the peaks of FTAN images and picking the prominent dispersion curve along with the average of all picked dispersion curves from 2-40 seconds to show their similarity to the reference. (C): Example FTAN image with picked phase velocity dispersion curve in green and the regional reference curve in black.

shape of the tree is controlled by the data and its associated uncertainty, with the scale of the uncertainty being controlled by a hierarchical scaling parameter that is also inverted for; thus the inversion does not require explicit regularization. The maximum number of parameters is therefore dictated by the highest level of the tree which, in this case is set to 7, a value that worked well in a comparable study by Pilia et al. (2020). For this region a maximum level of 7 would result in a minimum horizontal length scale of about 2 km; however the acceptance rate for parameters at this level is zero, indicating that the minimum length scale required by the data is larger and is thus not limited by this parameter choice.

The convergence of the Markov chain is aided by parallel tempering, where multiple chains at higher "temperature" are run in parallel with a primary chain, and exchanges permitted based on a probability calculated using the likelihood value of each model (Sambridge, 2014). The chains with higher temperatures will have an adjusted exchange probability that allows more variation in the model than the likelihood would typically allow, meaning that a wider set of models is sampled. This property, combined with exchanges with the primary chain, means that the final Markov Chain will be able to jump between local minima more easily and thus more efficiently search parameter space compared to a standard Markov Chain. Although this comes at the cost of extra computing resources required to run these chains in parallel, the time taken to run the same number of iterations remains similar. Using this method, we produced phase velocity maps for all periods of interest. For each period, we ran 8 parallel chains with 7 temperatures per chain for 2 million iterations and removed 750,000 iterations that accommodated a burn-in period. Each map took roughly 2.5 hours to produce on 448 CPUs, using 8 CPUs for each chain for each temperature, which we found to be the most computationally efficient distribution of resources. Once the ensemble of models was calculated, the final 2D phase velocity maps were generated from the average at every 20th iteration to avoid averaging correlated results. The advantage of using this method over other less computationally expensive methods (e.g. FMST, Rawlinson & Sambridge, 2004) include variable model resolution in the ensemble and posterior uncertainty estimates that can aid with the interpretation of results. Having variable resolution is particularly useful with this data set due to spatial variations in data coverage and quality (Figure 3a). While dispersion curves were extracted across most of the model, there were many station pairs for which the quality of the cross-correlations was not sufficient to obtain phase dispersion; this was particularly true for stations in the south east of the array. The input parameters controlling the inversion were tuned by performing various test runs at different periods and monitoring the acceptance rate of models and convergence of key parameters (e.g. likelihood, prior, hierarchical scaling, and number of model parameters). Monitoring the convergence of the number of model parameters was particularly useful since a similar distribution of parameters across all chains was a strong indicator of stability. More information on convergence can be found in the Supplementary Material.

2.4 Synthetic 2D tomography

In order to test the ability of our dataset to resolve lateral structure, we invert period-dependent inter-station path averaged velocity derived from a synthetic model for phase velocity structure. Here we choose the path coverage for 12 seconds period since it is representative across the full period range with an average number of ray paths. We produced a simple synthetic model consisting of blocks of different shapes, sizes and orientations perturbed by 10% from a background velocity of 3 km/s, and computed travel times through it by using the fast marching method implemented in the pykonal python package (White et al., 2020). This forward calculation takes into account ray bending to give more accurate travel times; however, the forward method used in the inversion scheme is based on computing path averaged velocity over a great circle. This means that the inversion will not be able to fit the synthetic data exactly, thus providing a more re-

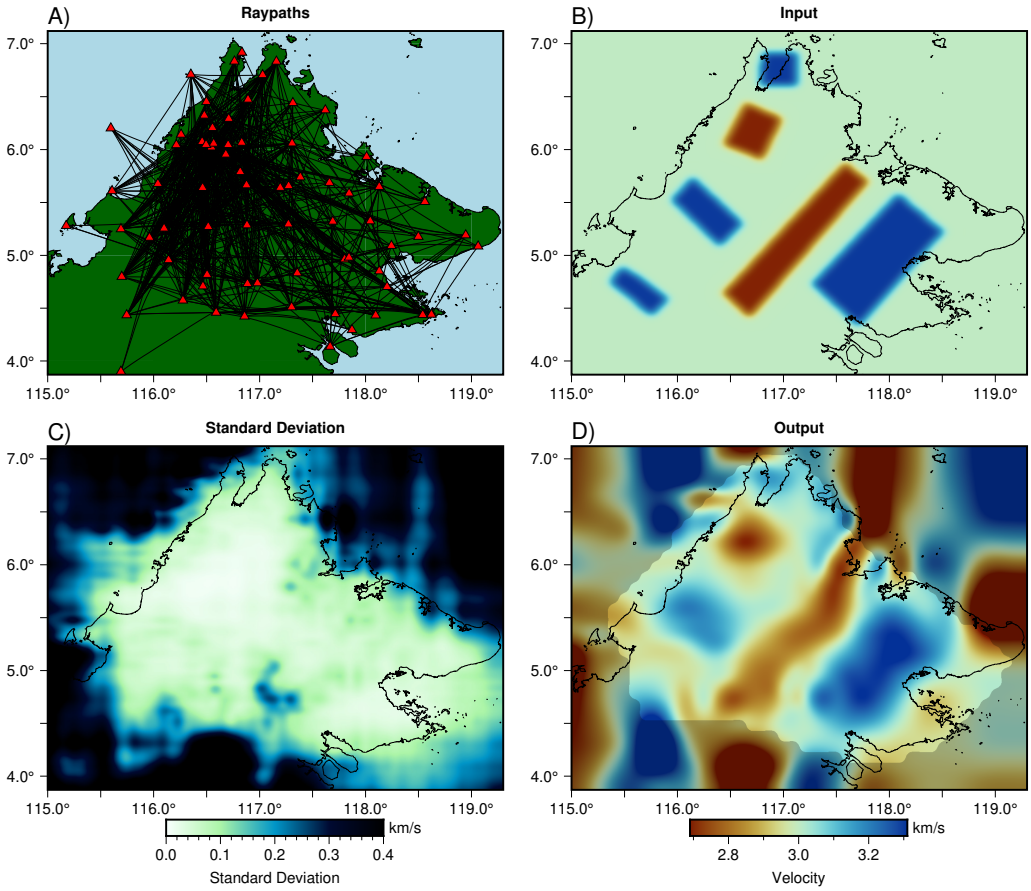

Figure 3. Results from the synthetic test using the 2D trans-dimensional trees tomographic method. (A): The location of the stations and the associated ray path coverage. (B) The input velocity model for the synthetic test. (C) The standard deviation of the ensemble produced by the rj-MCMC. (D) The recovered mean velocity model with a transparent mask to highlight the region of low uncertainty and hence robust recovery.

alistic view of the features that can be resolved. We then used the trans-dimensional trees method to reconstruct the model from calculated travel times with Gaussian noise of 0.3 s standard deviation added. The input model, ray paths and the mean and standard deviation map of the ensemble produced by the inversion are shown in Figure 3. The method does a good job of recovering the structure within the array; however, on the margin of the array there are many artefacts that could cause problems with any subsequent interpretation if not appropriately masked. The standard deviation map is very useful since it clearly shows that the uncertainty beyond the border of the array is considerably higher than within the array, so it is relatively straightforward to identify anomalies that are not interpretable. The underlying cause of the artefacts can be attributed to the bisecting rectangular parameterisation of the trans-dimensional trees method, where a few ray paths on the edge of the array are affecting the entire velocity model outside the array. In comparison, a trans-dimensional Voronoi cell parameterisation would tend to locate nodes within the array and hence the associated cells would be unlikely to span significant regions beyond the array boundary (Bodin et al., 2012b).

2.5 1D Inversion for S-wave velocity (Vs)

Once the 2D phase velocity maps are generated, the next step is to convert them into a 3D shear wave velocity model. This is achieved by sampling the period-dependent phase velocity maps on a grid of points to produce a corresponding set of pseudo dispersion curves, which can be separately inverted for 1D Vs structure. These models can then be combined into a single 3D Vs model. The method we use is described in Bodin et al. (2012a), although we did not exploit the capability of joint inversion with receiver functions and only inverted for 1D shear wave structure by using Rayleigh wave phase dispersion information. The 1D Vs inversion scheme also uses a rj-MCMC method that has hierarchical data error estimation in a data-driven approach for quantifying the appropriate data fit to the model. We ran this inversion on all 938 pseudo-dispersion curves that were sampled evenly in latitude and longitude with a grid spacing of 0.1 degree in the region of the mask shown in Figure 3, which was chosen on the basis of the standard deviation of the results from the 2D inversion. The grid spacing of 0.1 degree was chosen because it captured the smallest wavelength structure of the 2D models without adding unnecessary computation in the form of additional inversions. The output from this process was a depth dependent posterior distribution of Vs at each grid point from which the average and standard deviation was chosen as the final model and its associated uncertainty respectively. These 1D models were then used to construct a 3D shear wave velocity model by using 3D linear interpolation.

2.6 1D Inversion using an Artificial Neural Network

To help evaluate the robustness of our results, we tested an alternative method for inverting the pseudo-dispersion curves by using an Artificial Neural Network (ANN) that was applied in Yablokov and Serdyukov (2020) and adapted to suit this data set. To do so we created an ANN in the form of a simple vector to vector mapping that inputs a vector of phase velocity from a pseudo-dispersion curve and outputs a vector of shear wave velocity (Figure 4).

The network was first trained on a synthetic data set of 1D models produced by sampling 3D shear wave velocity models built from random perturbations to a 1D reference model based on the average interstation dispersion curve in our dataset. These random perturbations were drawn from a Gaussian distribution with 1 km/s standard deviation. The models were then smoothed both laterally by a Gaussian filter of 30 km width and in depth by a Gaussian filter of 5 km width to give more realistic models to train the network on. Phase velocity dispersion curves were calculated using the Computer Programs in Seismology (CPS) software (Herrmann, 2013) for each of the 1D models in the ensemble. This gave us a set of 5.4 million synthetic 1D shear wave velocity

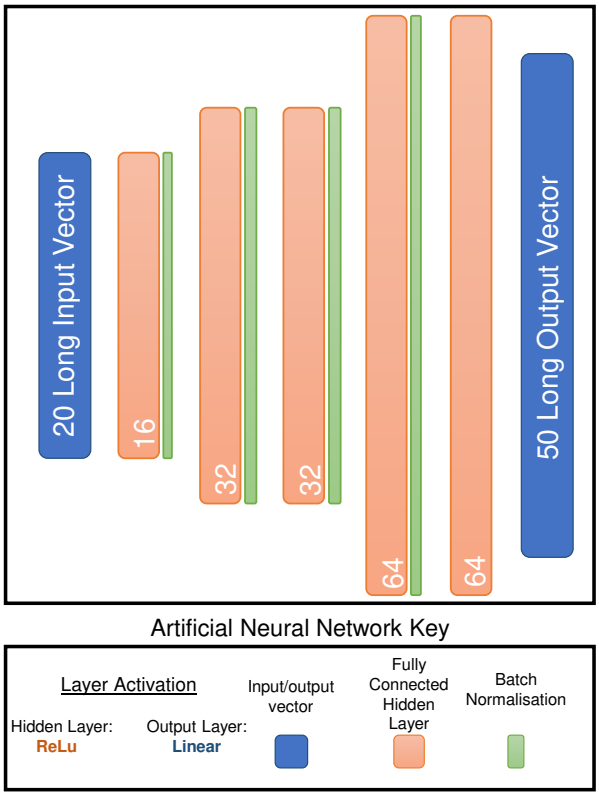

Figure 4. The architecture of the Artificial Neural Network used to perform the 1D inversions. The size of each fully connected layer and the input and output vector is written in each box along with the location of batch normalisation layers. The activation on all the hidden layers is a rectified linear unit (ReLu) and the activation on the output layer is linear.

models and associated Rayleigh phase velocity dispersion curves. The network was then trained on this output with 80% of the curves used to train the network and the remaining 20% to validate the network and ensure that we were not overfitting the data. The training was done with the ADAM optimiser with the learning rate set to the default value of 0.001 (Kingma & Ba, 2014) for 2000 epochs. The network was found to converge after 950 epochs when the minimum validation loss was found. This is the baseline network that approximates the inversion of phase velocity dispersion curves based on the synthetic data set. We then took the 1D models produced by the trans-dimensional method and performed transfer learning on our baseline network in order to update the model to include information about our region and the noise characteristics of the pseudo-dispersion curves. We again used an 80/20% train and validation split but this time the ADAM optimiser had the learning rate set to 5×10^{-5} and was trained for 1200 epochs. By using a learning rate 20 times smaller we try to ensure that the information learned by the network in the previous step is not forgotten and that any patterns in the noise on the real data are not learned by the model. The data set was much smaller for the transfer learning stage and therefore was very fast to compute making it feasible to run the training for 3000 epochs to ensure that even with the low learning rate it could converge on a reasonable solution. The test and training losses started to diverge at 2000 epochs so the final re-trained model was assumed to be optimum at that point.

The result of the above workflow is a network that provides a regionally localised approximate solution for the inverse problem as an application of the theorem that neural networks are universal approximators (Hornik et al., 1989). The reasoning for this is based on Yablokov and Serdyukov (2020), where they found that the neural network trained on synthetic data was much less sensitive to noise when performing inversions after training. This is a particularly useful feature of the method since many of the pseudo-dispersion curves contain unrealistic spikes or troughs in phase velocity due to the 2D inversions being performed separately; this means that there is no control on the lateral correlation of velocity anomalies between adjacent periods. When the neural network is re-trained on the pseudo-dispersion curves from the real data set after training by a synthetic data set, it will learn an approximate mapping for that region. When re-doing the inversion from pseudo-dispersion curve to 1D shear wave velocity with the re-trained ANN the result will be less sensitive to noise and unphysical changes in the dispersion curves. Using this method, all pseudo-dispersion curves were run on the final trained network to produce a new set of 1D velocity models that are used to construct a second 3D shear wave velocity model. This model is generally smoother and easier to interpret, although it is also helpful to consider the rj-McMC model in the interpretation, since many of the features are similar.

2.7 Synthetic 1D inversion results

We performed several synthetic tests for the 1D inversion scheme to determine how effective both of our methods are at resolving shear velocity from phase velocity dispersion curves. We used a model that extends in depth to 40 km with 1 km thick velocity layers that vary smoothly as a function of depth. The top 8 km features a gentle increase in velocity gradient with a homogeneous section between 8 and 18 km depth and a sharper velocity gradient between 18 and 25 km depth before changing back into a milder velocity gradient that extends to the base of our model. Although not identical to any model used for training the ANN, it is similar enough to expect that a good reconstruction is possible. We calculated the dispersion curve from the input model using CPS (Herrmann, 2013) and then added Gaussian noise with a 0.01 km/s standard deviation, which is a similar noise level to that of a good quality pseudo dispersion curve. We then ran it through both the TransD 1D inversion method and the ANN inversion method using the re-trained model as described above. Both results are shown in Figure 5.

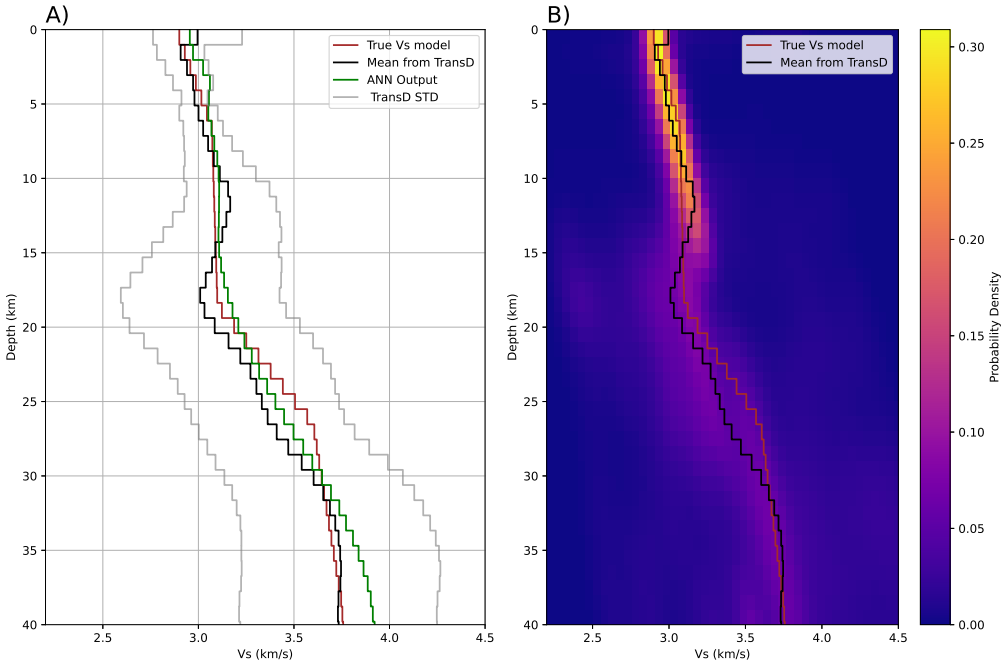

Figure 5. Results from a synthetic inversion for 1D structure. (A): 1D Vs models from the synthetic tests; the true model is in red, the average of the ensemble produced by the TransD method is in black with its associated standard deviation in gray and the result from the ANN method is in green. (B): The posterior PDF produced by the TransD method overlain by the TransD average in black and the true model in red.

The result from the synthetic TransD inversion include measurements of uncertainty and an output probability density map, shown in Figure 5B, representing the posterior distribution sampled by the Markov chain, which is used to produce the mean and standard deviation which we take to be the final 1D Vs model and its uncertainty. The TransD and ANN methods gives a very similar 1D profile to the true model, however, there are a few differences. Between 10 and 20 km depth in the model the TransD scheme has a tendency to overestimate the changes in velocity; this is most notable in Figure 5A at 12 and 18 km depth where the recovered TransD model has a positive and negative velocity anomaly respectively. This is not observed in the ANN model, which better matches the true velocity model in this region. For the sharper velocity gradient between 18 and 25 km depth, both the TransD and the ANN slightly underestimate the gradient but extends the feature over a greater depth range, which is typical of surface wave dispersion inversion. At 35-40 km the TransD model recovers the velocity quite well but the ANN model overestimates the velocity by up to 0.2 km/s. We expect this is likely due to the ANN not having seen a model quite like this since we do not see an overshoot at depth when comparing the final TransD and ANN models of the region. With the exception of the base of the model, the two different methods produce very similar results, which is to be expected since the ANN is designed as a preconditioned emulator of the TransD method.

3 Results

3.1 Phase velocity maps

Figure 6 shows the period-dependent phase velocity maps and standard deviations computed for 6, 16, 26 and 36 seconds. The velocity models adopt the mask that we used in the synthetics (Figure 3) due to the presence of similar edge effect issues. The standard deviation maps for these models show a consistent story with higher uncertainties in the east of the model, especially underneath the Dent peninsula, where ther is poorer ray path coverage and apparently noisier data. The region of the models under the Crocker Range has lower standard deviation that is consistently under 0.1 km/s and as such can be more reliably interpreted. There are also higher standard deviations located in the neighbourhood of strong lateral velocity contrasts even in regions that have good path coverage, such as the low velocity anomaly in the 6 second map in Figure 6A and B where the standard deviation rises to 0.3 km/s. This is due to the uncertainty around where to place such a contrast since there is a trade-off between the location, size and magnitude of the velocity change (Hawkins & Sambridge, 2015; Pilia et al., 2020), an effect perhaps more pronounced when using Voronoi cells (Pilia et al., 2015b).

3.2 Comparison of models produced by the two methods

To illustrate the difference between the two 1D inversion methods, we show a horizontal slice through the two final 3D models in Figure 7 with no smoothing applied. For long wavelength features, the two models look virtually identical, with low and high velocity anomalies found in the same place laterally and with depth. This is reassuring since it demonstrates that both methods agree that certain key features are required to fit the phase velocity maps. The models are more different at shorter scale lengths, with the ANN model showing a generally much smoother result both laterally and in depth compared to the TransD model. This is to be expected given the initial training of the ANN model on an ensemble of synthetic models, prior to transfer learning with the TransD inversion results. As a consequence, the 1D ANN inversion effectively features a higher degree of implicit smoothing regularisation yet is still capable of satisfying the data to the same extent. When compared to the picked phase velocity dispersion curves the model produced by the ANN has a residual mean of –0.057 km/s and residual standard deviation of 0.19 km/s whereas the model from the TransD method has a residual mean of

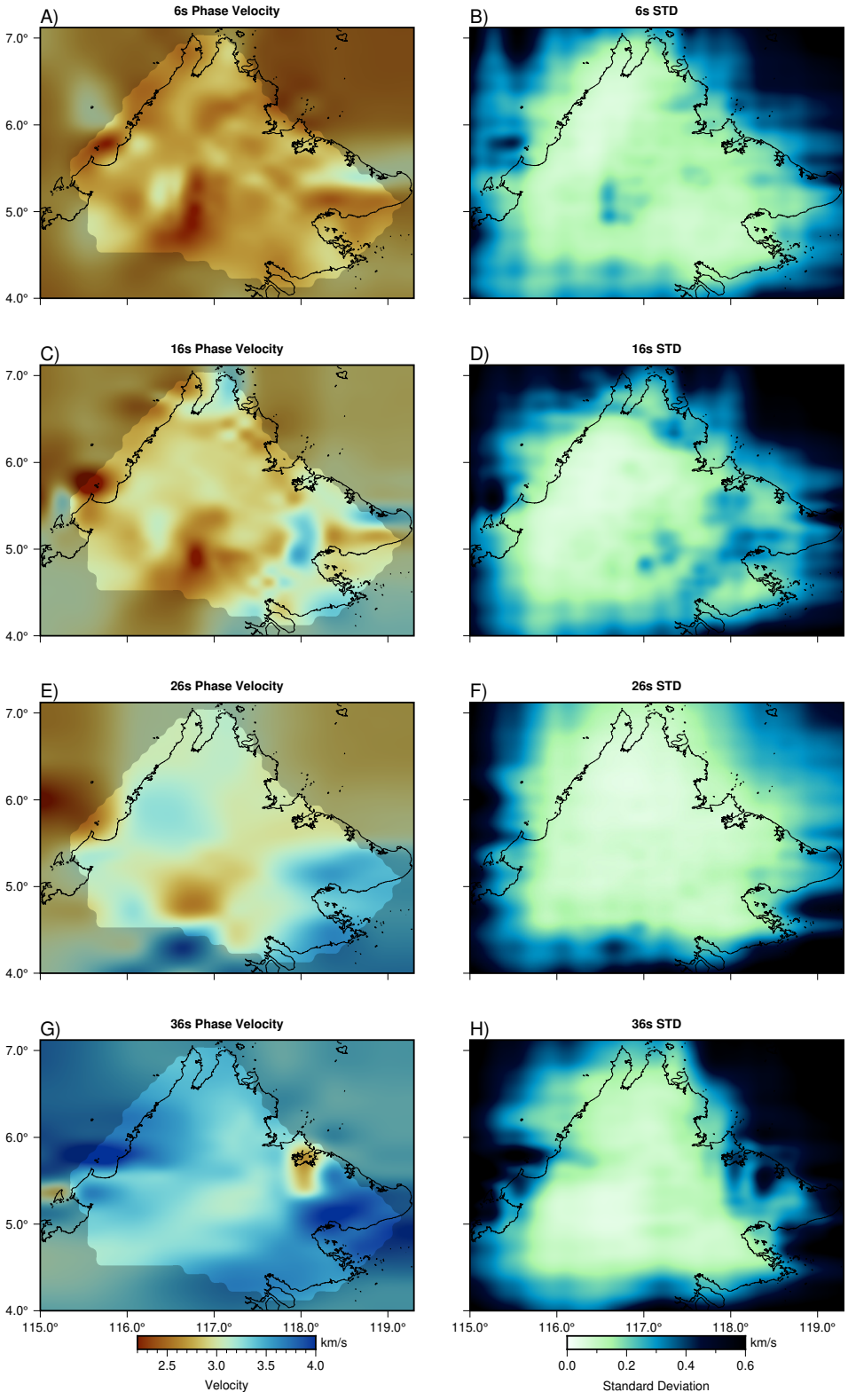

Figure 6. Example phase velocity maps and standard deviations produced by the trans-dimensional trees method. The velocity models are partially masked to show regions of lower standard deviation and improved recovery. Panels (A) and (B) show results for 6 s period, (C) and (D) for 16 s, (E) and (F) for 26 s and (G) and (H) for 36 s.

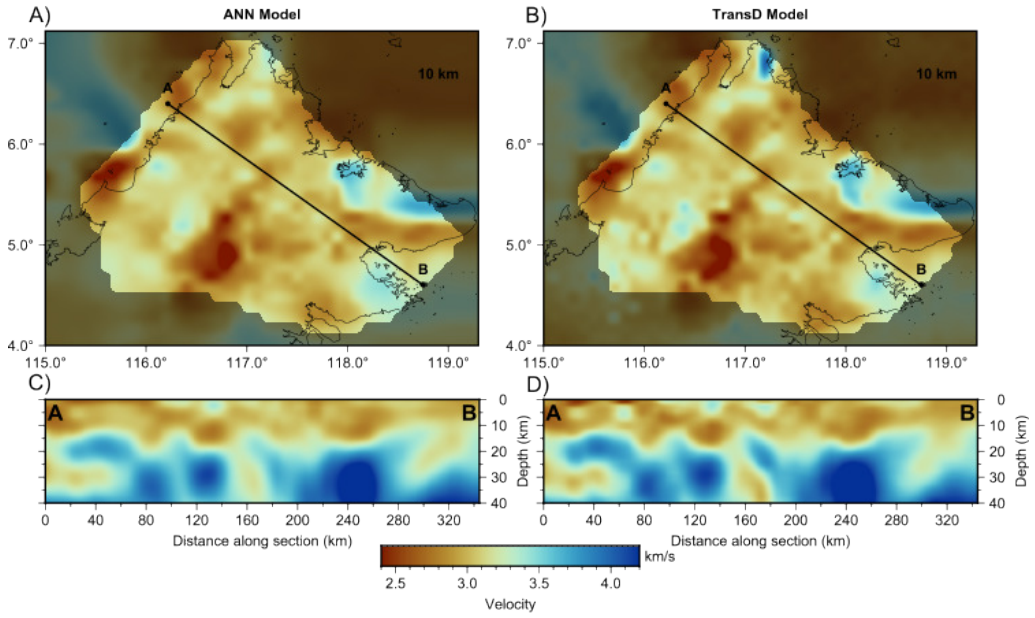

Figure 7. Horizontal slice at 10 km depth and cross-section from A to B for the final 3D shear wave velocity model produced by using the ANN method (left) and the TransD method (right).

–0.050 km/s and a residual standard deviation of 0.19 km/s. For this study we decided that the ANN model is more useful for interpretation since many of the short wavelength features are not resolvable by our level of data coverage and hence should not be considered.

3.3 Shear wave velocity model

The final composite 3D shear wave velocity model produced by the re-trained ANN 1D inversions is presented as a series of horizontal slices in the range 5-40 km depth (Figure 8) and cross sections through key sections of the model (Figure 9). Based on the synthetic inversions and the phase velocity maps, lateral features larger than 50 km are resolvable except in regions on the edge of the model where artefacts of the low coverage and trans-dimensional trees parameterisation appear. In some regions lateral resolution will be better, particularly in the region of the Crocker range where we have the most crossing rays. The lateral resolution will also reduce with increasing depth, since the ray path coverage at longer periods reduces, though there are fewer short wavelength structures visible below 20 km depth due to the trans-dimensional parameterisation reducing the length scale of features in the longer period phase velocity models. From the 1D synthetics, uncertainty generally increases with depth, but broadscale anomalies can still be reliably interpreted. The synthetics show that we do not resolve vertical contrasts very well and so we are unlikely to be able to accurately determine the dimensions of vertical anomalies. To ease interpretation, the model has been laterally smoothed using a Gaussian kernel with 10 km standard deviation. The text labels superimposed on Figures 8 and 9 highlight features that we will interpret in the discussion section.

In the upper 20 km of the crust, one of the more obvious features is the large Shallow Low Velocity (SLV) anomaly in the central southern region of the model (SLV1 on Figures 8 and 9). Here, velocities are as low as 2.5 km/s and the anomaly extends to ∼25 km depth. This feature underlies the Maliau Basin and other circular basins of Sabah,

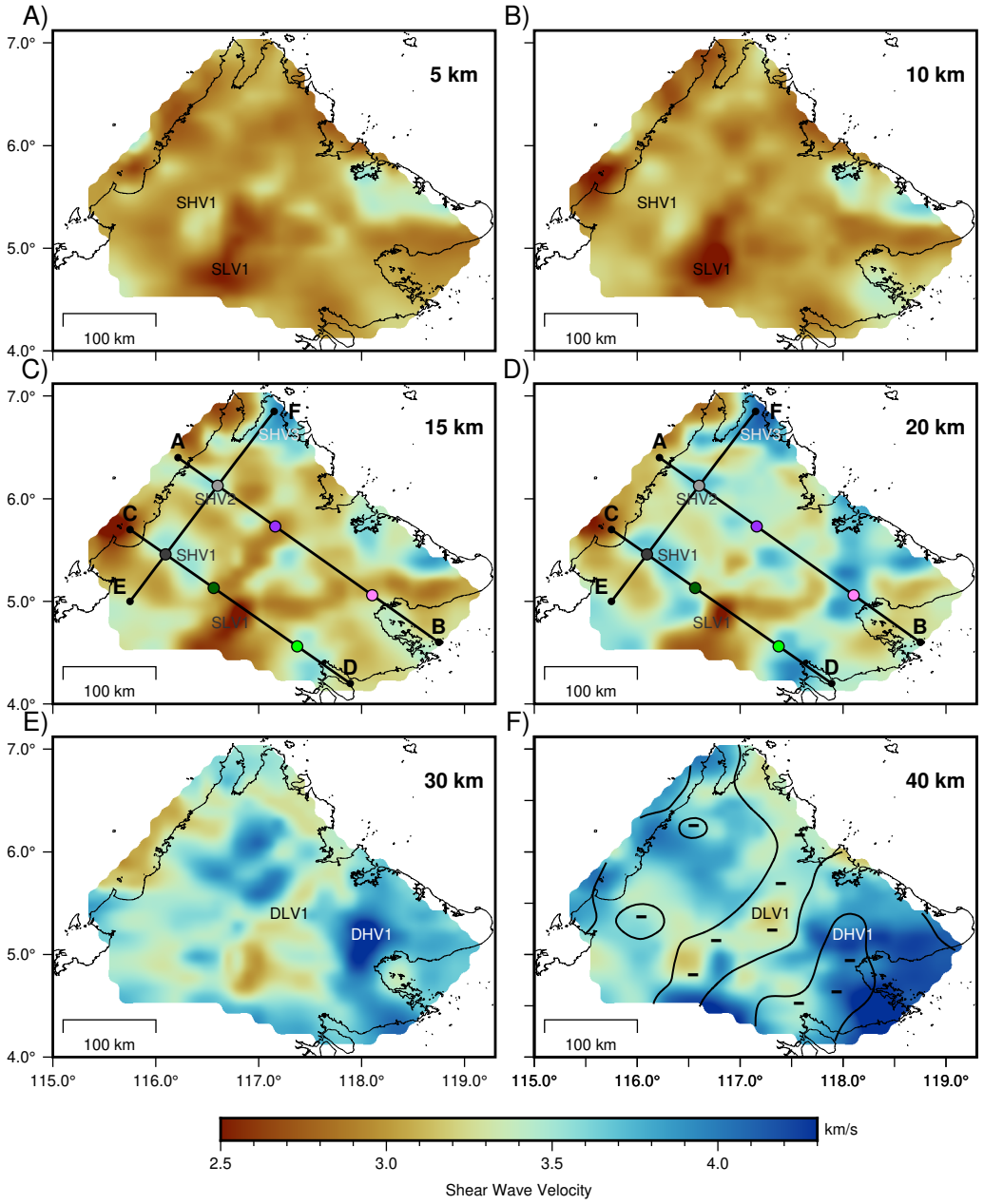

Figure 8. Horizontal slices from 5 to 40 km depth (Panels A-F) through the final shear wave velocity model produced by the re-trained ANN inversion. The three lines A-B, C-D and E-F are the locations of cross sections that are plotted in Figure 9. The velocity anomalies interpreted in the discussion section are also marked as SHV1, SHV2 and SLV1 for the shallow anomalies and DLV1 and DLV2 for the deep anomalies. The region of thinner crust found by Linang et al. (2022) is plotted on the 40 km depth slice as a single contour at 34 km depth.

so is likely a signature of low velocity sediments, although they are unlikely to extend that deep, suggesting that vertical smearing – an expected biproduct of surface wave inversion – is at play here. Previous estimates from structural geology, which themselves are not well constrained, have put the thickness of the Neogene sediments in this region at 6-7 km (Balaguru et al., 2003) so we may be seeing the effects of a very low velocity layer being smeared out by the bulk sampling of the surface waves measured in the ambient noise recordings. The upper mid-crust reveals a Shallow High Velocity (SHV) anomaly beneath the Crocker Range (SHV1 on Figures 8 and 9) of about 3.5-3.7 km/s extending from about 10 to 25 km depth. It is approximately 80 km long with a NW-SE strike that aligns with cross section C-D and is also visible in cross section E-F (Figure 9). This anomaly also seems to mark a difference in the topography between the northern and southern parts of the Crocker Range, which is an interesting correlation that will be discussed later. A second smaller high velocity anomaly exists under the Crocker Range beneath Mt Kinabalu (SHV2 on Figures 8 and 9); it is roughly cylindrical with a diameter of ∼40 km between depths of 15-25 km and has a maximum velocity of about 3.7 km/s, which is similar to SHV1. Finally a third high velocity anomaly labelled SHV3 is located in the north of the region; it extends from around 15 to 30 km depth and has velocities up to 3.8 km/s. SHV3 is the largest of these three shallow high velocity anomalies but is near the edge of the model so is not as well resolved when compared to SHV1 and SHV2.

Deeper in the model between 30-40 km depth, there is an intriguing pattern of NE-SW oriented high velocity anomalies in the southeast, low velocities in the centre and higher velocities in the northwest. This trend is primarily expressed in the long wavelength features of the model and also matches the central region of thin crust found by Linang et al. (2022), which is shown on Figure 8 as a 34 km depth contour from their crustal thickness model. The Deep Low Velocity (DLV) band featuring velocities of 3.2-3.4 km/s in the centre of Sabah and striking NE-SW extends southwest from the northeast coast and is about 200 km long and 40 to 80 km wide. It is most clearly seen in the 40 km depth slice in Figure 8F and cross section AB in Figure 9A where it is marked as DLV1. There is also a Deep High Velocity (DHV) anomaly with values ranging between 4.1-4.2 km/s that covers much of eastern Sabah marked as DHV1 in Figures 8E/F and 9A. The peak velocities of this anomaly are mostly concentrated around Darvel Bay between the Dent and Semporna peninsulas, but it covers most of the eastern part of our region at depth. It is worth noting that the uncertainty in this region is higher than elsewhere, especially on the Dent peninsula (Figure 6), but it is likely that we can still resolve larger scale high velocity anomalies at this depth, especially under the Semporna peninsula where the values of uncertainty are generally lower.

4 Discussion

4.1 Complex crustal structure in western Sabah

The crust beneath the Crocker Range lies in the most well constrained region of our model according to the standard deviation maps and synthetic inversion results (Figure 3). It also contains several unexpected complexities in a region that has relatively simple mapped surface geology as shown in Hall (2013), with much of the area being covered by Cretaceous-Lower Miocene sediments and more recent Pleistocene sediments. The complexity we see in the 10 to 20 km depth range of the shear-wave velocity model is manifest in the presence of SHV1, SHV2 and SHV3 along with SLV1 located further southeast beneath the Maliau Basin. Figure 10 shows a 10 km depth slice through this section of the model alongside a map of topography with the locations of SHV1, SHV2, SHV3 and SLV1 highlighted. The subduction of the Proto-South China Sea (PSCS) is believed to have occurred in this region (Hall, 2013), as supported by recent evidence of a relict slab that traverses the NW coast in the mid-lower upper mantle from teleseismic travel time tomography (Pilia et al., 2023a, 2023b). The subsequent collision and

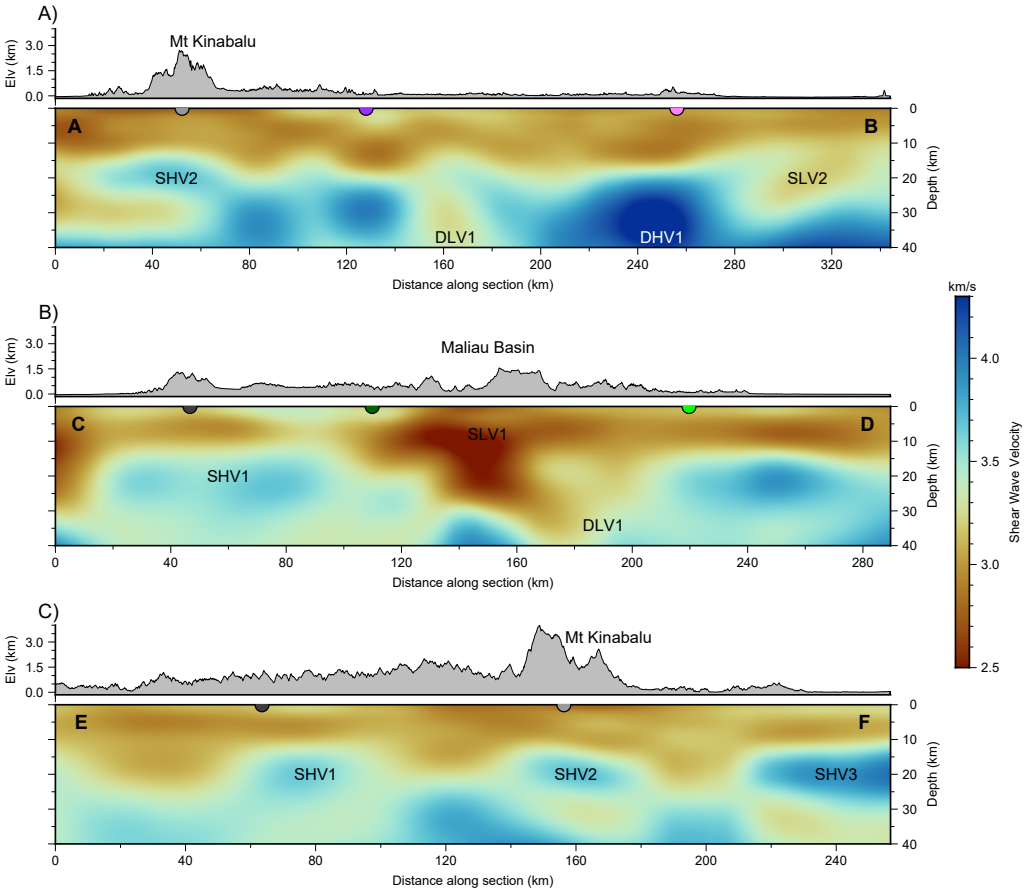

Figure 9. Cross sections through the final shear wave velocity model produced by the re-trained ANN inversion and the elevation (Elv) of the topography along the section. The locations of the cross sections are shown in Figure 8. Cross section A-B in panel A transects Mt Kinabalu, which can be seen in the elevation, as well as the interpreted anomalies SHV2, DLV1 and DHV1. Cross section C-D in panel B runs through the Maliau Basin, which shows up as the shallow low velocity anomaly SLV1 and also converges on anomalies SHV1 and DLV1. Cross section E-F in panel C runs along strike of the Crocker Range and through the anomalies SHV1, SHV2 and SHV3.

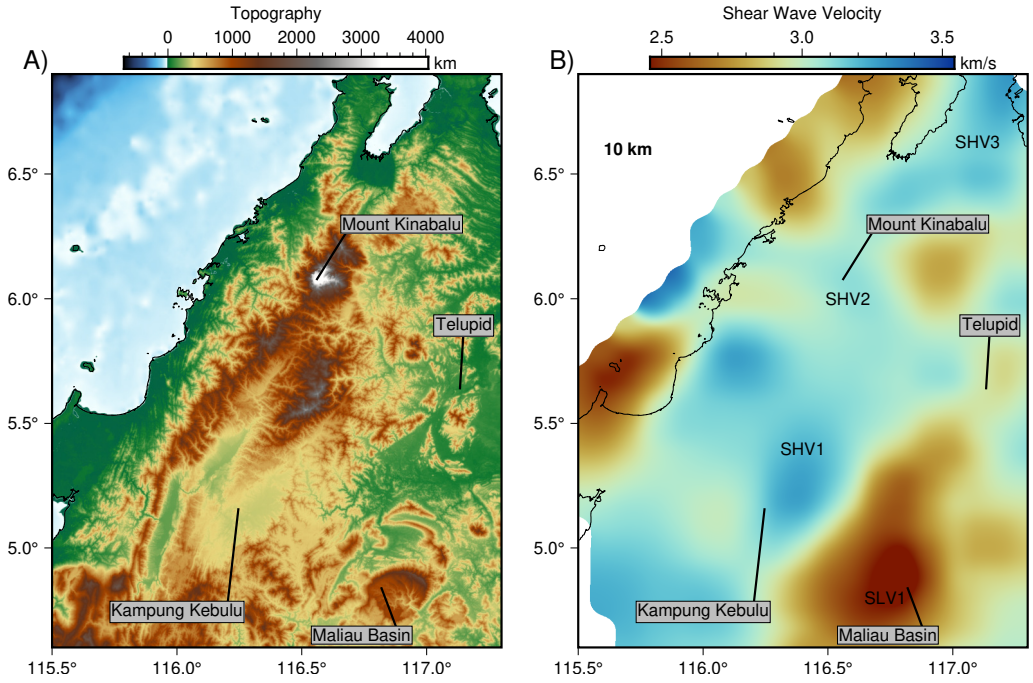

Figure 10. Surface topography and a 10 km depth slice from our final shear wave velocity model showing the shallow anomalies in relation to surface features. SHV1 is located under a region of low topography in the Kampung Kebulu area, SHV2 is located underneath Mount Kinabalu and SLV1 is located underneath Maliau Basin. The depth slice is plotted with a different colour scale than Figure 8 and 9 and is centred on the mean shear wave velocity at 10 km depth to better highlight the anomalies we see in this section of the model.

underthrusting of the Dangerous Grounds block is believed to be the reason for the termination of the subduction of PSCS (Hall, 2013). The three high velocity anomalies and the lower velocities that underlay them are, therefore, possible evidence of the underthrusting of heterogeneous continental crust from the collision of the Dangerous Grounds block producing along strike variations in velocity structure. This variation was also observed by Gilligan et al. (2023) who sees similar regions of high and low velocity anomalies in the crust along the Crocker Range from inversion of receiver functions for shear wave velocity structure. If these anomalies are associated with underthrusting, it is likely that the high velocity structures represent the lower portion of what was the overriding crust, and the low velocities beneath represent the upper part of the underthrust Dangerous Grounds crust.

The velocity anomaly at the southern edge of the Crocker Range, SHV1, also coincides with a region of flat topography that marks a clear difference in relief between the mountainous regions to the north and south (Figure 10). This topographic low could be caused by heavy erosion followed by infill of younger Pliocene/Pleistocene sediment (<5 Ma) (Hall, 2013). This would explain the apparent thinning of the low velocity layer in the upper crust as seen in Figure 9B. However, another option, supported by the presence of SHV1, is the existance of rigid material under this section of the Crocker Range that resisted deformation or limited it to the narrow band near the coast as seen in the topography. A similar structure is seen in the Iberian Peninsula in the form of the Ebro block, which is a continental block within the compressional margin of the Pyrenees that shows a region of thin crust and lower relief surrounded to the north and south by thicker crust and higher relief (King et al., 2023). This is in a comparable tectonic setting with

similar topography to what we see on this segment of the Crocker Range, though the scale of the Pyrenees is larger.

The second high velocity anomaly in western Sabah is located under Mt Kinabalu (SHV2). This is a much smaller anomaly than SHV1 in both depth and lateral extent and lies beneath a region of anomalously high topography. This high velocity anomaly is most clearly seen in cross section A-B (9) and in Figure 10, which show it extending down to 20 km depth and underlain by a lower velocity zone. Mt Kinabalu is a large granite pluton that was intruded into Mesozoic igneous and metamorphic rocks and Cenozoic sediments (Cottam et al., 2010) and then extension caused exhumation of a sub-continental peridotite suite (Tsikouras et al., 2021). It is therefore likely that SHV2 and the smaller high velocity zone beneath Telupid represents this ultramafic material that is also found at the surface in this area (Hall, 2013). The third high velocity anomaly in the very north of our model, SHV3, is much larger and has a higher amplitude than SHV1 and SHV2. It is in a region of our model that has relatively poor coverage and therefore has the potential to suffer from edge effects. However, a very similar structure has been imaged by Gilligan et al. (2023), suggesting that it is real, though its exact dimensions are likely to be poorly constrained. The position of the SHV3 anomaly coincides with a clear shift in the fabric of the region, with southwest-northeast striking features to the south in the Crocker Range to more east-west fabric on the northern tip of Borneo, as seen in the topography map in Figure 10A. This change in fabric is interpreted to be the result of collision with the Reed Bank in the north (Tongkul, 1994). The Reed Bank is another continental block within the South China sea that collided with Palawan to the north. Tongkul (1994) suggests that this region has undergone uplift as a result of this collision, so the shallow high velocities could be evidence of uplifted ultramafic material near the surface.

4.2 Evidence for extensive melting and subduction in Sabah

In eastern Sabah between 20-40 km depth, the velocities are higher than anywhere else in the model region – see anomaly DHV1 in Figures 8 and 9. The Dent and Semporna peninsulas are characterised by Miocene island arc magmatism, with samples dated between 16-9 Ma (Lai et al., 2021; Bergman et al., 2000), which is thought to be the result of Celebes Sea subduction that occurred immediately to the southeast. Subsequently, the Semporna peninsula experienced magmatic episodes from 4-2 Ma that exhibit an ocean island basalt type signature (Macpherson et al., 2010), which has since been related to possible lithospheric delamination directly beneath (Pilia et al., 2023b; Greenfield et al., 2022). It is therefore possible that the high velocities beneath eastern Sabah represent plutonic mid-lower crust that may have formed due to melting, as first suggested by Hall (2013). The shallowest point of the DHV1 anomaly is also co-located with the exposed ultramafic material of the Darvel Bay ophiolite (Hall, 2013). If the higher velocities do represent a plutonic crustal layer, then it appears to shallow between the Semporna and Dent peninsulas, though this is hard to quantify given the uncertainty limiting our resolution in the east, particularly under the Dent peninsula.

A notable feature adjacent to DHV1, which is most visible in cross section AB in Figure 9A, is a low velocity anomaly (SLV2) that extends down to ∼35 km depth and has a slight dip to the northwest. This anomaly is located on the edge of our region of low standard deviation that ranges from around 0.1 km/s beneath the Semporna peninsula to 0.4 km/s beneath the Dent peninsula, thus requiring any interpretation to be made with a certain degree of caution. However, given its moderate dip and location, it may be a signature of underthrust sediment or duplexes at the former subduction front of the Celebes Sea Slab, consistent with what is observed in the study of Zhang and Miller (2021) in a similar setting. If so, it would represent the first geophysical evidence of Celebes Sea subduction, though further work is required to support this interpretation, particularly in light of the limited data coverage in this region of the model.

4.3 Sabah failed rift from Celebes Sea subduction rollback

Near the base of our model at 40 km depth, the anomaly DLV1 in Figures 8 and 9 shows a band of low velocity stretching from the Sulu Sea to the Maliau Basin. This low velocity anomaly coincides with a region of thin crust found by applying Virtual Deep Seismic Sounding (VDSS) on the same data set as this study (Linang et al., 2022). VDSS resolves the Moho discontinuity (as shallow as ∼20 km in this part of northern Borneo), whereas ANT using surface waves can only recover smooth velocity variations as a function of depth. As a consequence, the two sets of results are not directly comparable, but one could be expected to see low velocities in rifted crust due to a thermal anomaly (Accardo et al., 2020).

In Linang et al. (2022), this region of crustal thinning is explained as a continuation of the extension of the opening of the Sulu Sea caused by the rollback of the Celebes Sea Slab, which at the time subducted NW beneath northern Borneo. When the subduction ceased at 9 Ma, the extension stopped leaving a region of thinned crust. The idea of continued extension of the Sulu Sea on land in northern Borneo was first suggested by Hall (2013) and was corroborated by Tsikouras et al. (2021), who found Miocene zircons in the mafic rocks at Telupid and Ranau. In Tsikouras et al. (2021) these were used to suggest that extension led to the exhumation of a sub-continental peridotite suite near Ranau and a rift-related magmatic episode near Telupid. Whether these zircons were magmatic or metasomatic due to their presence in mafic/ultra-mafic rocks was questioned by Cullen and Burton-Johnson (2021). We suggest that the DLV1 anomaly and its very strong correlation with the region of thin crust seen in Linang et al. (2022) supports the idea that late Miocene extension occurred under northern Borneo, thus producing an upwelling of warmer material into the region left by the thinned crust. The anomaly DLV1 is also mildly asymmetrical and dipping towards the southwest, which matches up with numerical simulations of continental rift initiation where asymmetrical features of this type have been observed (Brune et al., 2014). Pilia et al. (2015a) invoked a similar explanation when they discovered a low velocity anomaly beneath the failed rift in Bass Strait, Southeast Australia. This was interpreted as a residual thermal upwelling initiated by thinning during extension. Invoking a similar mechanism here supports the model of late Miocene extension due to rollback of the Celebes Sea slab and is consistent with other evidence of a failed rifting episode (Tsikouras et al., 2021; Linang et al., 2022). As a simple check of the validity of this interpretation, we calculated the characteristic thermal relaxation time of a thermal anomaly at 40 km depth in the Earth's crust using the following calculation (Michaut et al., 2007).

$$\tau = \frac{L^2}{\kappa} \tag{1}$$

where τ is the characteristic thermal relaxation time, L is the length scale and κ is the thermal diffusivity of the crust. By taking the length scale to be 40 km, which is the depth to the velocity anomaly, and a range of realistic thermal diffusivities, we can calculate a range of characteristic thermal relaxation times. We use thermal diffusivities that span 7.0×10^{-3} - 15.0×10^{-3} $cm^2 s^{-1}$ to represent extreme differences in crustal composition found in Seipold and Gutzeit (1982). This gives us a range of relaxation times from 33-72 million years, which means that if extension ceased at approximately 9 Ma, then insufficient time has passed to significantly dissipate the resultant thermal anomaly produced by the extension (Chenin et al., 2020). While compositional variations cannot be ruled out to explain our observations, higher temperatures associated with relatively recent failed rifting appears to be the most likely explanation.

5 Conclusions

We have imaged the shear wave velocity structure of the crust beneath northern Borneo to a depth of 40 km using ambient noise tomography applied to data from the

nBOSS array collected between 2018 and 2020. We apply a two step inversion method using Trans-dimensional Trees for the 2D step and a combination of Trans-dimensional inversion and a new artificial neural network based inversion for the 1D inversion step. The new ANN inversion was shown to be effective at recovering heterogeneous structure and produced a smoother model than the transD method while still satisfying the data. From this new crustal shear wave velocity model, complex subsurface structure beneath the Crocker Range is discovered containing various high velocity anomalies that are interpreted to be evidence of underthrusting of Dangerous Grounds continental crust that feature significant along-strike variations. High velocities in east Sabah reveal evidence of significant melting due to the subduction of the Celebes Sea slab and subsequent decompression melting. In the east a low velocity anomaly may indicate the presence of underthrust sediments or duplexes that support Celebes Sea subduction, though resolution is limited. We find evidence of Sulu Sea extension – likely caused by Celebes Sea subduction – propagating southwest into northern Borneo to ultimately produce a failed continental rift. This is in the form of a low velocity anomaly that may be the signature of elevated temperatures that persist following the cessation of failed rifting. Furthermore, we illuminate the subsurface structure of the Maliau Basin and reveal a thick low velocity anomaly that likely represents a thick sedimentary sequence that formed prior to the emergence of the eastern part of northern Borneo following Celebes Sea slab breakoff. Further work on this region could include the extraction and inversion of Love wave dispersion data, the joint inversion of receiver functions and surface wave dispersion, and the inclusion of longer period dispersion data extracted from teleseismic events.

Data Availability Statement

The nBOSS dataset is accessible through the IRIS Data Management service (https://www.fdsn.org/networks/detail/YC_2018/). Data from the Malaysian national seismic network (https://www.fdsn.org/networks/detail/MY/) are restricted but may be obtained by contacting the Malaysian Meteorological Department. The stacked cross correlations produced as part of this study are available at doi:10.6084/m9.figshare.25360090

Acknowledgments

The authors wish to thank all those who were involved in deploying, servicing and recovering the nBOSS network between March 2018 and January 2020, including the land owners of Sabah who hosted seismometers. The seismometers used were provided by the Natural Environment Research Council (NERC) Geophysical Equipment Facility through SeisUK (loan 1038) as well as the University of Cambridge and the University of Aberdeen (Aberdeen University Geophysical Equipment Repository – AUGER). Thanks are also extended to MetMalaysia for providing access to their continuous waveform data recorded by their MY network in Sabah. J.F. was supported by a studentship funded jointly by the Engineering and Physical Sciences Research Council (EPSCR) and CGG. We acknowledge the use of several free python packages in this work including pykonal (White et al., 2020), obspy (Beyreuther et al., 2010), matplotlib (Hunter, 2007), pytorch (Paszke et al., 2019), xarray (Hoyer & Hamman, 2017) and pyGMT (Wessel et al., 2019).

References

Accardo, N. J., Gaherty, J. B., Shillington, D. J., Hopper, E., Nyblade, A. A., Ebinger, C. J., ... Class, C. (2020, 6). Thermochemical modification of the upper mantle beneath the northern malawi rift constrained from shear velocity imaging. *Geochemistry, Geophysics, Geosystems*, *21*, e2019GC008843. doi: 10.1029/2019GC008843

Almeida, J., Riel, N., Rosas, F. M., Duarte, J. C., & Schellart, W. P. (2022, 1). Polarity-reversal subduction zone initiation triggered by buoyant plateau

obstruction. *Earth and Planetary Science Letters*, *577*, 117195. doi: 10.1016/J.EPSL.2021.117195

Bacon, C. A., Rawlinson, N., Pilia, S., Gilligan, A., Wehner, D., Cornwell, D. G., & Tongkul, F. (2022, 11). The signature of lithospheric anisotropy at post-subduction continental margins: New insight from xks splitting analysis in northern borneo. *Geochemistry, Geophysics, Geosystems*, *23*, e2022GC010564. doi: 10.1029/2022GC010564

Balaguru, A., Nichols, G., & Hall, R. (2003, 5). The origin of the 'circular basins' of sabah, malaysia. *Bulletin of the Geological Society of Malaysia*, *46*, 335-351. doi: 10.7186/bgsm46200355

Bergman, S. C., S., H. C., Swauger, D. A., & Graves, J. E. (2000, 7). K:ar ages and geochemistry of the sabah cenozoic volcanic rocks. *Bulletin of the Geological Society of Malaysia*, *44*, 165-171. doi: 10.7186/bgsm44200021

Beyreuther, M., Barsch, R., Krischer, L., Megies, T., Behr, Y., & Wassermann, J. (2010, 5). Obspy: A python toolbox for seismology. *Seismological Research Letters*, *81*, 530-533. doi: 10.1785/gssrl.81.3.530

Bodin, T., Sambridge, M., Rawlinson, N., & Arroucau, P. (2012b, 6). Transdimensional tomography with unknown data noise. *Geophysical Journal International*, *189*, 1536-1556. doi: 10.1111/j.1365-246X.2012.05414.x

Bodin, T., Sambridge, M., Tkalćić, H., Arroucau, P., Gallagher, K., & Rawlinson, N. (2012a, 2). Transdimensional inversion of receiver functions and surface wave dispersion. *Journal of Geophysical Research: Solid Earth*, *117*. doi: 10.1029/2011JB008560

Brune, S., Heine, C., Pérez-Gussinyé, M., & Sobolev, S. V. (2014, 6). Rift migration explains continental margin asymmetry and crustal hyper-extension. *Nature Communications*, *5*, 1-9. doi: 10.1038/ncomms5014

Chenin, P., Schmalholz, S. M., Manatschal, G., & Duretz, T. (2020, 7). Impact of crust–mantle mechanical coupling on the topographic and thermal evolutions during the necking phase of 'magma-poor' and 'sediment-starved' rift systems: A numerical modeling study. *Tectonophysics*, *786*, 228472. doi: 10.1016/j.tecto.2020.228472

Cottam, M., Hall, R., Sperber, C., & Armstrong, R. (2010, 1). Pulsed emplacement of the mount kinabalu granite, northern borneo. *Journal of the Geological Society*, *167*, 49-60. doi: 10.1144/0016-76492009-028

Cullen, A., & Burton-Johnson, A. (2021, 11). New zircon radiometric u-pb ages and lu-hf isotopic data from the ultramafic-mafic sequences of ranau and telupid (sabah, eastern malaysia): Time to reconsider the geological evolution of southeast asia? *Geology*, *49*, 541-541. doi: 10.1130/G49414C.1

Gilligan, A., Cornwell, D., Rawlinson, N., Tongkul, F., Pilia, S., Greenfield, T., & Bacon, C. (2023). Imaging subduction, collision, and extension in northern borneo: Constraints from receiver function. *EarthArXiv*. doi: 10.31223/X5BT2J

Green, P. J. (1995, 12). Reversible jump markov chain monte carlo computation and bayesian model determination. *Biometrika*, *82*, 711-732. doi: 10.1093/BIOMET/82.4.711

Greenfield, T., Gilligan, A., Pilia, S., Cornwell, D. G., Tongkul, F., Widiyantoro, S., & Rawlinson, N. (2022, 2). *Post-subduction tectonics of sabah, northern borneo, inferred from surface wave tomography* (Vol. 49). John Wiley and Sons Inc. doi: 10.1029/2021GL096117

Hall, R. (1996). Reconstructing cenozoic se asia. *Geological Society Special Publication*, *106*, 153-184. doi: 10.1144/GSL.SP.1996.106.01.11

Hall, R. (2013, 10). Contraction and extension in northern borneo driven by subduction rollback. *Journal of Asian Earth Sciences*, *76*, 399-411. doi: 10.1016/j.jseaes.2013.04.010

Hall, R., & Spakman, W. (2015). Mantle structure and tectonic history of se asia.

Tectonophysics, *658*, 14-45. doi: 10.1016/j.tecto.2015.07.003

Hanasoge, S. M. (2013, 1). The influence of noise sources on cross-correlation amplitudes. *Geophysical Journal International*, *192*, 295-309. doi: 10.1093/gji/ggs015

Hawkins, R., & Sambridge, M. (2015). Geophysical imaging using trans-dimensional trees. *Geophysical Journal International*, *203*, 972-1000. doi: 10.1093/gji/ggv326

Herrmann, R. B. (2013, 11). Computer programs in seismology: An evolving tool for instruction and research. *Seismological Research Letters*, *84*, 1081-1088. doi: 10.1785/0220110096

Hornik, K., Stinchcombe, M., & White, H. (1989, 1). Multilayer feedforward networks are universal approximators. *Neural Networks*, *2*, 359-366. doi: 10.1016/0893-6080(89)90020-8

Hoyer, S., & Hamman, J. (2017). xarray: N-d labeled arrays and datasets in python. *Journal of Open Research Software*, *5*. doi: 10.5334/jors.148

Hunter, J. D. (2007). Matplotlib: A 2d graphics environment. *Computing in Science Engineering*, *9*, 90-95. doi: 10.1109/MCSE.2007.55

Hutchison, C. S., Bergman, S. C., Swauger, D. A., & Graves, J. E. (2000, 7). A miocene collisional belt in north borneo: uplift mechanism and isostatic adjustment quantified by thermochronology. *Journal of the Geological Society*, *157*, 783-793. doi: 10.1144/JGS.157.4.783

King, M. T., Welford, J. K., & Tugend, J. (2023, 3). The role of the ebro block on the deformation experienced within the pyrenean realm: Insights from deformable plate tectonic models. *Journal of Geodynamics*, *155*, 101962. doi: 10.1016/j.jog.2023.101962

Kingma, D. P., & Ba, J. L. (2014, 12). Adam: A method for stochastic optimization. *3rd International Conference on Learning Representations, ICLR 2015 - Conference Track Proceedings*. doi: 10.48550/arxiv.1412.6980

Laat, J. I. D., Lebedev, S., Celli, N. L., Bonadio, R., Melo, B. C. D., & Rawlinson, N. (2023, 7). Structure and evolution of the australian plate and underlying upper mantle from waveform tomography with massive data sets. *Geophysical Journal International*, *234*, 153-189. doi: 10.1093/gji/ggad062

Lai, C. K., Xia, X. P., Hall, R., Meffre, S., Tsikouras, B., Balangue-Tarriela, M. I. R., ... aqidah Norazme, N. (2021, 2). Cenozoic evolution of the sulu sea arc-basin system: An overview. *Tectonics*, *40*, e2020TC006630. doi: 10.1029/2020TC006630

Lecocq, T., Caudron, C., & Brenguier, F. (2014). Msnoise, a python package for monitoring seismic velocity changes using ambient seismic noise. *Seismological Research Letters*, *85*, 715-726. doi: 10.1785/0220130073

Linang, H. T., Pilia, S., Rawlinson, N., Bacon, C. A., Gilligan, A., Cornwell, D. G., & Tongkul, F. (2022, 10). Collision-induced subduction polarity reversal explains the crustal structure of northern borneo: New results from virtual deep seismic sounding (vdss). *Geophysical Research Letters*, *49*. doi: 10.1029/2022GL099123

Luo, Y., Yang, Y., Xu, Y., Xu, H., Zhao, K., & Wang, K. (2015, 5). On the limitations of interstation distances in ambient noise tomography. *Geophysical Journal International*, *201*, 652-661. doi: 10.1093/gji/ggv043

Macpherson, C. G., Chiang, K. K., Hall, R., Nowell, G. M., Castillo, P. R., & Thirlwall, M. F. (2010, 2). Plio-pleistocene intra-plate magmatism from the southern sulu arc, semporna peninsula, sabah, borneo: Implications for high-nb basalt in subduction zones. *Journal of Volcanology and Geothermal Research*, *190*, 25-38. doi: 10.1016/j.jvolgeores.2009.11.004

Michaut, C., Jaupart, C., & Bell, D. R. (2007, 4). Transient geotherms in archean continental lithosphere: New constraints on thickness and heat production of the subcontinental lithospheric mantle. *Journal of Geophysical Research: Solid*

Earth, *112*. doi: 10.1029/2006JB004464

Morley, C. K., & Back, S. (2008, 1). Estimating hinterland exhumation from late orogenic basin volume, nw borneo. *Journal of the Geological Society*, *165*, 353-366. doi: 10.1144/0016-76492007-067

Morley, C. K., King, R., Hillis, R., Tingay, M., & Backe, G. (2011, 1). Deep-water fold and thrust belt classification, tectonics, structure and hydrocarbon prospectivity: A review. *Earth-Science Reviews*, *104*, 41-91. doi: 10.1016/J.EARSCIREV.2010.09.010

Paszke, A., Gross, S., Massa, F., Lerer, A., Bradbury, J., Chanan, G., ... Chintala, S. (2019, 12). Pytorch: An imperative style, high-performance deep learning library. *Advances in Neural Information Processing Systems*, *32*. doi: 10.48550/arXiv.1912.01703

Pilia, S., Davies, D. R., Hall, R., Bacon, C. A., Gilligan, A., Greenfield, T., ... Rawlinson, N. (2023b, 7). Post-subduction tectonics induced by extension from a lithospheric drip. *Nature Geoscience*, *16*, 646-652. doi: 10.1038/s41561-023-01201-7

Pilia, S., Jackson, J. A., Hawkins, R., Kaviani, A., & Ali, M. Y. (2020, 2). The southern zagros collisional orogen: New insights from transdimensional trees inversion of seismic noise. *Geophysical Research Letters*, *47*. doi: 10.1029/2019GL086258

Pilia, S., Rawlinson, N., Cayley, R. A., Bodin, T., Musgrave, R., Reading, A. M., ... Young, M. K. (2015b, 2). Evidence of micro-continent entrainment during crustal accretion. *Scientific Reports*, *5*, 1-6. doi: 10.1038/srep08218

Pilia, S., Rawlinson, N., Direen, N. G., Reading, A. M., Cayley, R., Pryer, L., ... Duffett, M. (2015a, 10). Linking mainland australia and tasmania using ambient seismic noise tomography: Implications for the tectonic evolution of the east gondwana margin. *Gondwana Research*, *28*, 1212-1227. doi: 10.1016/j.gr.2014.09.014

Pilia, S., Rawlinson, N., Gilligan, A., & Tongkul, F. (2019, 5). Deciphering the fate of plunging tectonic plates in borneo. *Eos*, *100*. doi: 10.1029/2019eo123475

Pilia, S., Rawlinson, N., Hall, R., Cornwell, D. G., Gilligan, A., & Tongkul, F. (2023a, 3). Seismic signature of subduction termination from teleseismic p- and s-wave arrival-time tomography: The case of northern borneo. *Gondwana Research*, *115*, 57-70. doi: 10.1016/J.GR.2022.11.014

Rawlinson, N., & Sambridge, M. (2004). Wave front evolution in strongly heterogeneous layered media using the fast marching method. *Geophysical Journal International*, *156*, 631-647. doi: 10.1111/J.1365-246X.2004.02153.X

Sambridge, M. (2014, 1). A parallel tempering algorithm for probabilistic sampling and multimodal optimization. *Geophysical Journal International*, *196*, 357-374. doi: 10.1093/GJI/GGT342

Seipold, U., & Gutzeit, W. (1982, 7). The distribution of thermal diffusivity in the earth's crust. *Physics of the Earth and Planetary Interiors*, *29*, 69-72. doi: 10.1016/0031-9201(82)90139-X

Tang, Q., & Zheng, C. (2013, 1). Crust and upper mantle structure and its tectonic implications in the south china sea and adjacent regions. *Journal of Asian Earth Sciences*, *62*, 510-525. doi: 10.1016/j.jseaes.2012.10.037

Tongkul, F. (1994, 7). The geology of northern sabah, malaysia: Its relationship to the opening of the south china sea basin. *Tectonophysics*, *235*, 131-147. doi: 10.1016/0040-1951(94)90021-3

Tongkul, F. (1997, 1). Polyphase deformation in the telupid area, sabah,malaysia. *Journal of Asian Earth Sciences*, *15*, 175-183. doi: 10.1016/S0743-9547(97)00006-8

Tsikouras, B., La, C. K., Ifandi, E., Norazme, N. A., Teo, C. H., & Xia, X. P. (2021, 7). New zircon radiometric u-pb ages and lu-hf isotopic data from the ultramafic-mafic sequences of ranau and telupid (sabah, eastern malaysia):

Time to reconsider the geological evolution of southeast asia? *Geology*, *49*, 789-793. doi: 10.1130/G48126.1

Ventosa, S., Schimmel, M., & Stutzmann, E. (2017). Extracting surface waves, hum and normal modes: time-scale phase-weighted stack and beyond. *Geophysical Journal International*, *211*, 30-44. doi: 10.1093/gji/ggx284

Volk, O. (2020). Velocity and anisotropy structure of the icelandic crust: An ambient seismic noise analysis. *Apollo - University of Cambridge Repository*.

Volk, O., White, R. S., Pilia, S., Green, R. G., Maclennan, J., & Rawlinson, N. (2021, 3). Oceanic crustal flow in iceland observed using seismic anisotropy. *Nature Geoscience*, *14*, 168-173. doi: 10.1038/s41561-021-00702-7

Wang, L., Dai, L., Gong, W., Li, S., Jiang, X., Foulger, G., ... Yu, S. (2022, 2). Subduction initiation at the solomon back-arc basin: Contributions from both island arc rheological strength and oceanic plateau collision. *Geophysical Research Letters*, *49*, e2021GL093369. doi: 10.1029/2021GL097666

Wehner, D., Blom, N., Rawlinson, N., Daryono, Böhm, C., Miller, M. S., ... Widiyantoro, S. (2022, 3). Sassy21: A 3-d seismic structural model of the lithosphere and underlying mantle beneath southeast asia from multi-scale adjoint waveform tomography. *Journal of Geophysical Research: Solid Earth*, *127*, e2021JB022930. doi: 10.1029/2021JB022930

Wessel, P., Luis, J. F., Uieda, L., Scharroo, R., Wobbe, F., Smith, W. H. F., & Tian, D. (2019, 11). The generic mapping tools version 6. *Geochemistry, Geophysics, Geosystems*, *20*, 5556-5564. doi: 10.1029/2019GC008515

White, M. C., Fang, H., Nakata, N., & Ben-Zion, Y. (2020, 7). Pykonal: A python package for solving the eikonal equation in spherical and cartesian coordinates using the fast marching method. *Seismological Research Letters*, *91*, 2378-2389. doi: 10.1785/0220190318

Yablokov, A., & Serdyukov, A. (2020, 1). Inversion of surface waves dispersion curves using artificial neural network. *Conference: 82nd EAGE Annual Conference Exhibition Workshop Programme*, 1-5. doi: 10.3997/2214-4609.202010809

Yao, H., van Der Hilst, R. D., & de Hoop, M. V. (2006). Surface-wave array tomography in se tibet from ambient seismic noise and two-station analysis — i. phase velocity maps. *Geophysical Journal International*, *166*, 732-744. doi: 10.1111/j.1365-246X.2006.03028.x

Zenonos, A., De Siena, L., Widiyantoro, S., & Rawlinson, N. (2020, 5). Direct inversion of s-p differential arrival times for vpvs ratio in se asia. *Journal of Geophysical Research: Solid Earth*, *125*, e2019JB019152. doi: 10.1029/2019JB019152

Zhang, P., & Miller, M. S. (2021, 2). Seismic imaging of the subducted australian continental margin beneath timor and the banda arc collision zone. *Geophysical Research Letters*, *48*. doi: 10.1029/2020GL089632